Solid Freeform Fabrication 2024: Proceedings of the 35th Annual International Solid Freeform Fabrication Symposium – An Additive Manufacturing Conference
Reviewed Paper

GRADIENT SEGMENTATION OF IN-SITU INFRARED IMAGES IN ELECTRON BEAM POWDER BED FUSION

B. Johnstone*, C. Saldana*

* George W. Woodruff School of Mechanical Engineering, Georgia Institute of Technology, Atlanta, GA 30332

Abstract

In order for metal additive manufacturing to be more effectively and widely used in industry, greater process control is needed. One way to achieve this is through the use in-situ process monitoring, such as using layer-wise infrared imaging to detect porosity in electron beam powder bed fusion. Due to the pores having more emissivity than the solid part, they appear brighter in infrared images and can therefore be detected by using image processing techniques. This work compares how applying different image filtering and gradient types can detect these brighter spots correlating to developing pores. Results were both qualitatively assessed using image appearance and histogram distributions and quantitatively assessed using pixel-to-pixel comparison to x-ray computed tomography scans. Gradients that use larger kernel sizes (specifically three-by-three) were more accurate in detecting porosity, and this was further aided by a gaussian or anisotropic diffusion filter.

1. Introduction

****

Metal additive manufacturing (AM) has seen a significant rise in use in both industry and research settings due to its ability to create parts with numerous freedoms (such as geometry, microstructure, etc.) that are not available with other manufacturing methods [1][2]. However, since AM is significantly newer than traditional manufacturing processes, these processes have less understanding, especially with quality control [3]. Therefore, in-situ process monitoring has been implemented in both industrial and research applications. These types of process monitoring systems have been used to detect various defects in different metal AM processes such as laser powder bed fusion (PBF-LB) and electron beam powder bed fusion (PBF-EB). These defects include geometric defects (such as geometric accuracy [4], high surface roughness [5], and dross formation [6]), powder bed defects (such as short coating [7], hopping [8], and streaking [9]), and porosity [10]. Detecting these defects is critical because their presence can impact the parts overall performance, such as reducing tensile strength [11] or fatigue strength [12].

To accomplish this, a variety of sensors have been used. Some sensors include acoustic sensors [13], ultrasonic sensors [14], accelerometers [15], and photodiodes [16]. Imaging, both visible-light [17] and infrared-light spectrum [18], is one of the more common sensor types due to its ease of use and processing. Infrared (IR) imaging is effective for detecting heat-related defects such as porosity in PBF processes. This is especially true for PBF-EB because pores are caused by buildups of heat energy in unmelted sections that give off excess IR thermal radiation and therefore appear as bright spots in IR images [19]. Previous researchers have used IR imaging to detect pores [20], understand how they form [21], and measure the reaction to interlayer cool time [10].

Since the IR cameras export data in the form of images, numerous image processing techniques have been applied to extract relevant data from the images. Due to the pores appearing as bright spots in the IR images, thresholding has been a common processing technique. Global thresholds, which use a preset grayscale value have been used to detect temperatures above a certain value [22] and to fine regions for further analysis of porosity formation [23]. Statistical thresholds, which calculate a threshold for each image using the distribution of grayscale values, have been used for porosity detection [24]. Another common technique is detecting gradients in the IR images, since the pore pixels will be significantly brighter than the surrounding solid part [25]. Finally, machine learning (ML) algorithms have been applied to these types of images. These algorithms often use the grayscale values alongside feature-based methods (such as identifying certain shapes) [26], but these methods are typically used for more complicated detection applications, such as distinguishing between lack of fusion and keyholing porosity [27] or determining porosity alongside other defects such as surface roughness [28]. However, it should be noted that ML methods require training time and significant computing power compared to the more basic image processing methods.

Finally, to verify the validity of these in-situ process monitoring systems, ex-situ evaluation has been used. The growing field of non-destructive evaluation (NDE) has provided numerous opportunities for measuring part quality without damaging them, allowing the parts to be used later or reevaluated if necessary. One NDE method that has seen high use in AM is X-ray computed tomography (XCT) [29]. XCT has been used to verify porosity formation in numerous systems including pyrometry [30], both optical [31] and near-IR imaging [32], and multi-sensor fusion systems [33].

However, with all this previous work, two main gaps remain. First, for using these image processing techniques, there is a notable lack of optimization for this use case both from how to determine the gradient and how to preprocess the images for segmentation. Second, most instances using a ground-truth measurement for verification have used manual, subjective registration, having the user align the datasets, especially in PBF-EB. This work aims to address both gaps by 1) using a rigorous, feature-based registration process to align the in-situ test dataset and the ex-situ reference dataset, and 2) using the registration to quantitatively evaluate the effectiveness of 5 different gradient methods (Sobel, Prewitt, Central, Intermediate, and Roberts) with 4 different prefilters (no filter, median filter, gaussian filter, and anisotropic diffusion filter). Each of these combinations of gradients and prefilters were qualitatively observed and quantitatively evaluated for their effect on successfully detecting and measuring porosity. XCT scans of the parts served as a ground-truth reference, using a sufficiently small voxel size to properly detect porosity and evaluate the gradient segmentation process. Insights from these results give future researchers and machine operators a greater understanding of how each of these gradients and filters affect the accuracy of detecting porosity from in-situ IR images.

2. Methods

****

2.1 Sample Design and Manufacturing

Samples were manufactured on an *ARCAM Spectra L* out of Ti-6Al-4V using ARCAM theme 6.1.12 and a layer thickness of 70 μm. To create varying levels of porosity, the focus offset

(FO) was varied to 55, 65, and 75 mA, as increasing FO has a correlation with generating porosity from the literature [21]. 9 samples were manufactured for each FO for a total of 27 samples. Samples were organized in the build layout in groups of 9 samples (3 of each FO) as shown in Figure 1. All samples were designed as cylinders with a flat vertical surface to facilitate registration of IR and XCT datasets (Figure 2).

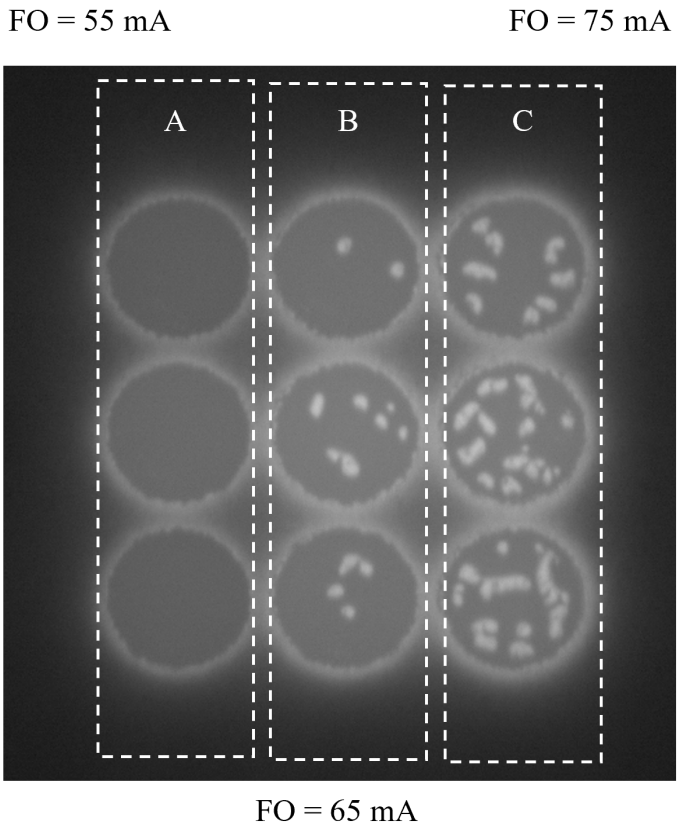

Figure 1: IR image showing layout of samples within each grouping of 9 samples with A) 3 samples with FO = 55 mA, B) 3 samples with FO = 65 mA, and C) 3 samples with FO = 75 mA

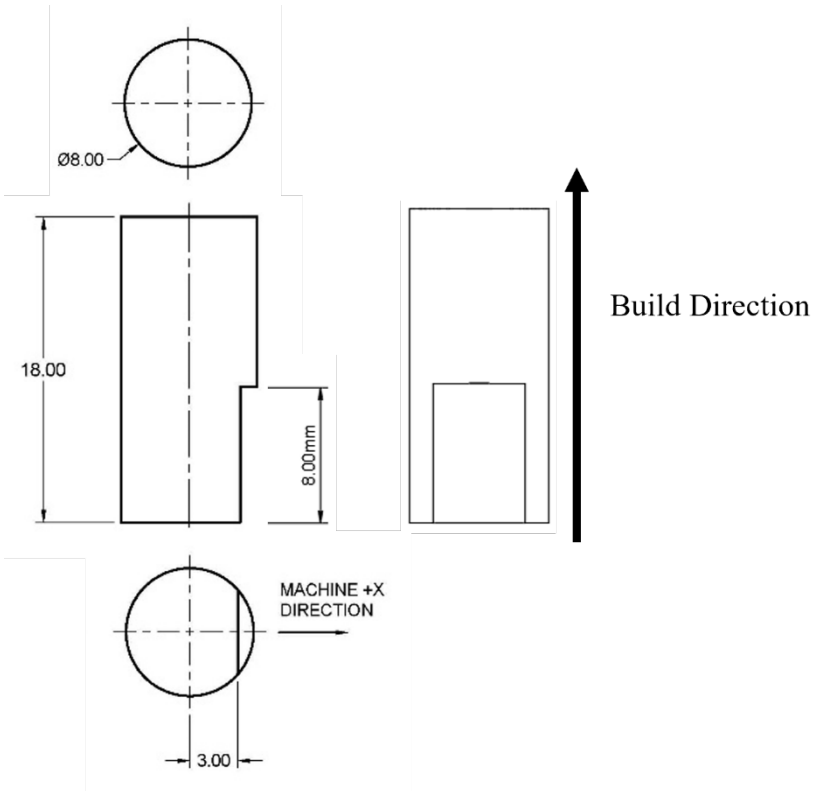

Figure 2: Sample design with registration features

2.2 X-Ray Computed Tomography Scanning and Processing

Manufactured samples were XCT scanned on a *Zeiss Metrotom 800 XCT*. A nylon fixture (low x-ray attenuation) was used to ensure all scans were in the same orientation using a voltage of 130 kV, current of 61 μA, a 0.25 mm copper filter, and 1600 projections. The resulting scan had a voxel size of 12 μm. After being reconstructed using a Feldkamp-David-Kress reconstruction algorithm and Shepp-Logan digital filter [34], registration was performed using MATLAB code developed by the research team. First, a surface was generated by segmenting the material grayscale values from the air using an ISO-50 threshold. Then, points on the surface were sampled in the cylindrical section. A cylinder was fitted to these points, and the central axis of this cylinder became the primary datum. Next, points were sampled on the vertical face, and a plane was fitted to these points. The perpendicular axis became the secondary datum. Finally, points were sampled on the top face, and another plane was fitted to these points, which became the tertiary datum. Using these datums, a rotation matrix was calculated.

Once registration was performed, the XCT images were segmented using Weka 3D segmentation in ImageJ [35]. This program allows the user to manually classify pixels that are used to train a machine learning algorithm to apply to future images. A training set of images was created using images from each sample's image stack. After each round of training, the results were manually evaluated for accuracy and retrained if necessary. Classes used were Solid Part, Pore, Fixture, and Air. To reduce noise, a Gaussian convolution with window sizes of 1, 2, 4, and 8 voxels. Once the operator deemed the model sufficiently trained and correctly identifying pixels,

it was applied to the remaining images for segmentation [36]. An example of this is shown in Figure 7.

2.3 Infrared Imaging and Gradient Segmentation

IR images were taken at the end of each layer with the original equipment manufacturer supplied IR camera. This camera used a prime lens with a focal length of 350 mm and an infrared-radiation sensor with a bit depth of 8 bits. The images taken were 5120 x 5120 pixels with a resolved pixel size of 70 µm within the field of view. Images were corrected for distortion using the pinhole camera model program in MATLAB 2022a. After this preprocessing, each image was cropped to a single sample, resulting in stacks of images of size 137 x 137 pixels (Figure 3a). Next, one of 4 image filters were applied: no filter, median filter, gaussian filter, or anisotropic diffusion filter. Then, one of 5 gradient determination methods were applied: Sobel, Prewitt, Intermediate, Central, or Roberts. This produced a set of gradient images (Figure 3b). However, since some of the gradient methods produced small gradients, each gradient image was rescaled to make the gradient values spanned the range of 0 to 1 (Figure 3c). These rescaled gradient images were then binarized with a threshold value determined via the Otsu method [37] (Figure 3d). Since the gradients only found the boundaries of the pores, an image filling algorithm was performed to capture the entirety of the pores (Figure 3e). Finally, the binarized image stacks were resized to match the registered XCT image stack and aligned using a marker pixel for pixel-to-pixel comparison. All image processing was performed in MATLAB 2022a.

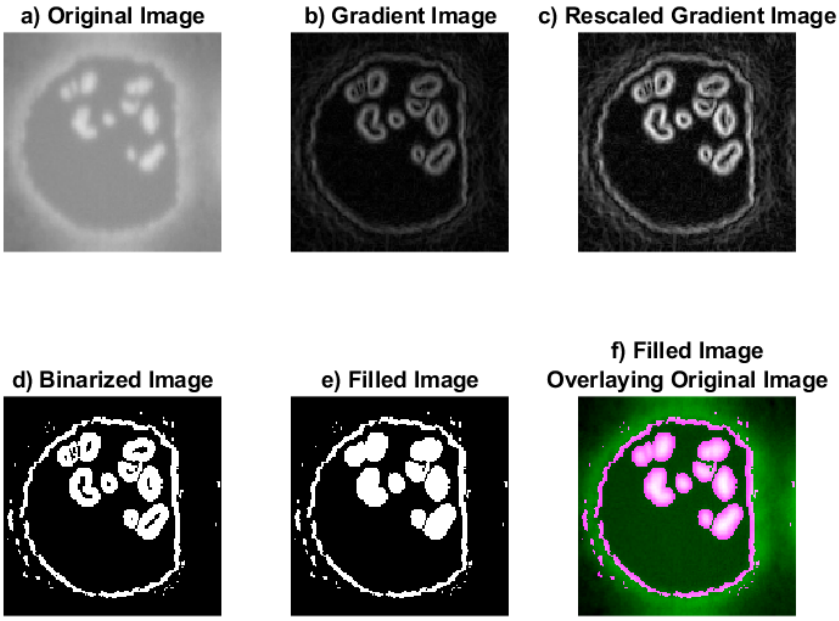

Figure 3: Workflow layout with a) original cropped image, b) gradient-applied image, c) gradient image rescaled to be between 0 and 1, d) binarized gradient image, e) binarized imaged with pores filled in, and f) filled image overlaying original image

2.4 XCT to IR Comparison

Once both image stacks were processed, a set of comparison images was generated via subtracting the pixel values of the IR images from 2 times the pixel values of the XCT images (2

* XCT - IR). Then, each value was given a different red-blue-green (RGB) color value based on the classification accuracy value: green for True Positive (TP), grey for True Negative (TN), red for False Negative (FN), and blue for False Positive (FP). Pixels outside the part boundary (determined by being outside the Solid Part boundaries in the Weka-classified images) were colored black to distinguish from the actual TN pixels.

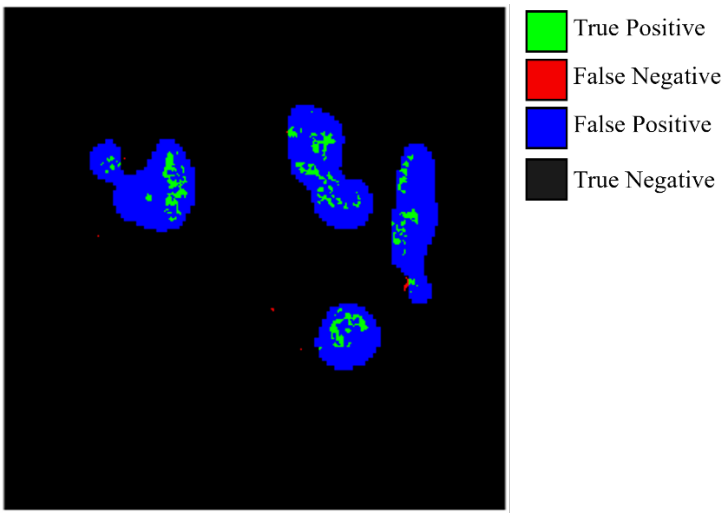

Figure 4: Example of Colorized Comparison Image

3. Results

****

3.1 Manufacturing and XCT Scanning

All samples were manufactured successfully, and the chosen FO values created consistent and significantly different levels of porosity. This was observed in both the IR images, such as those in Figure 1, and the CT images, such as those in Figure 5. Additionally, as Figure 6 shows, the registration process successfully aligned the two datasets. It should be noted that the pores in the IR images are significantly larger than the pores in the XCT images. This was due to two factors. First, the IR images were taken with a larger resolution (70 µm compared to the 12 µm of the XCT images), so the IR images were less precise. Second, since the IR images measure IR radiation and the images were taken while the pores were still hot, some heat likely spread out to the surrounding areas. This means those surrounding areas, where pores did not form, still gave off additional IR radiation and made the pores appear larger in the IR images. These two factors mean that pixel-to-pixel correlations appeared less accurate, as the IR pores were larger and oversized compared to the ground-truth reference.

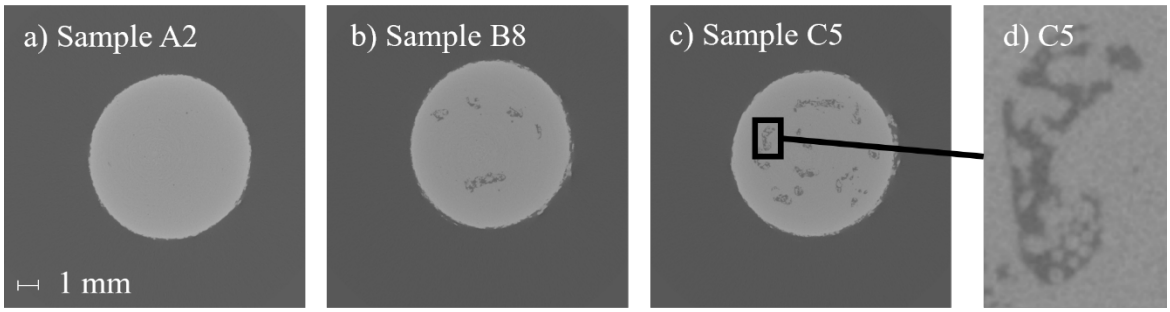

Figure 5: Raw XCT images showing varying porosity levels for a) sample A2 (low porosity), b) sample B8 (medium porosity), and c) sample C5 (high porosity). d) a zoomed-in view of a pore from sample C5.

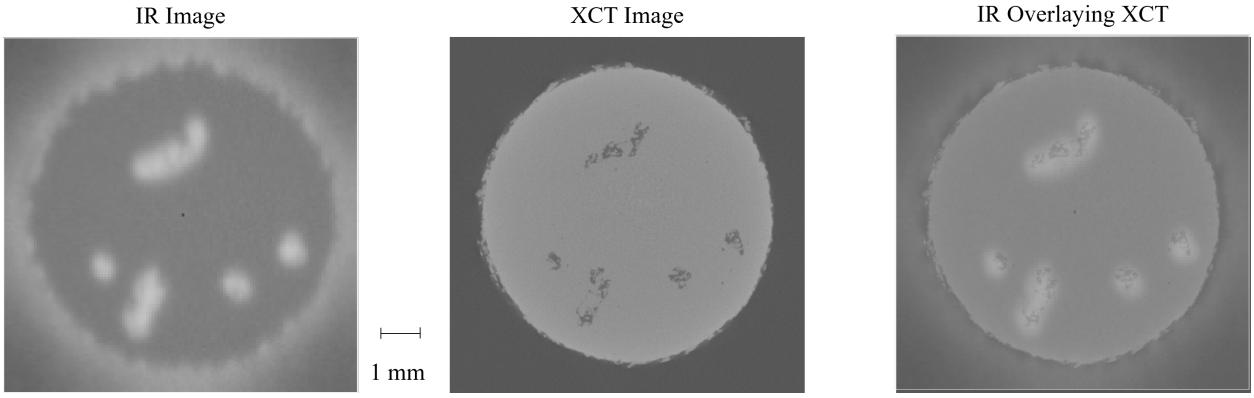

Figure 6: Comparing results of a) registered IR image and b) registered XCT image, with c) IR image overlaying XCT image

As described in Section 2.2, the XCT images were segmented using a 3D Weka supervised learning segmentation program. The results of this process are shown in Figure 7. As seen in the figure, the model successfully segmented between the 4 different classes and accurately represented the porosity.

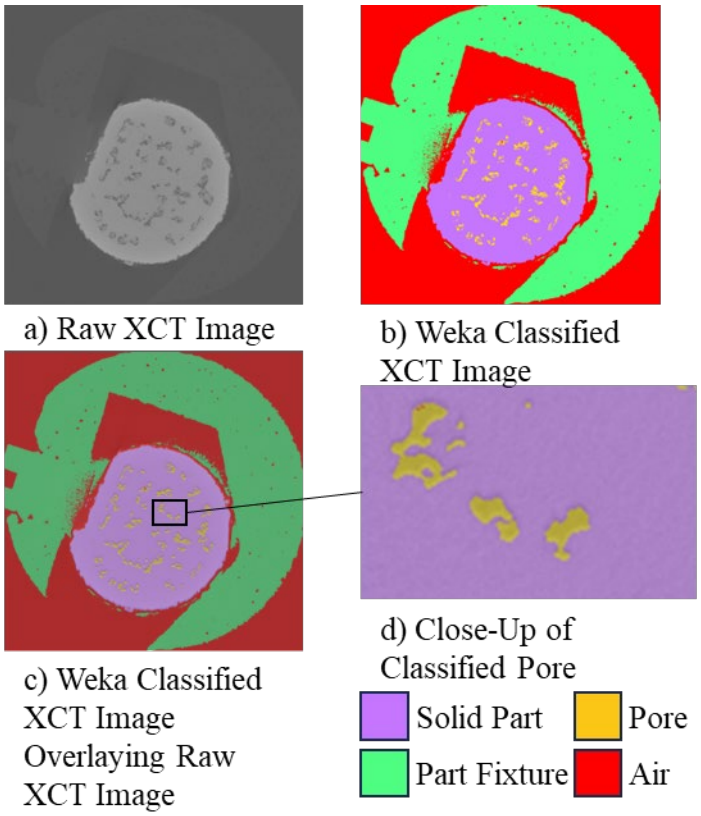

Figure 7: Example of Weka classified XCT Image with a) raw XCT image, b) Weka classified image, c) Weka classified image overlaying raw XCT image, and d) zoomed-in overlay

3.2 Gradient – Qualitative

Results from applying different gradients can be qualitatively observed in Figure 7. The different gradients gave slightly different magnitudes and distributions. First, in the gradient images in row a), the Sobel and Prewitt gradient images in a-i) and a-ii), respectively, had noticeably less noise than the Intermediate and Roberts gradient images in a-iv) and a-v), respectively. This was especially noticeable in regions without pores. Additionally, the Sobel and Prewitt gradients produced larger gradients, as shown by the brighter gradient images. Second, the Sobel and Prewitt gradients also resulted in smoother histograms, seen in b-i) and b-ii), respectively, than the other gradients in b-iii), b-iv), and b-v). These other gradients resulted in varying levels of large changes in grayscale counts between neighboring grayscale values, resulting in areas of higher threshold sensitivity (where smaller changes in the threshold value resulted in classifying larger collections of pixels). However, in most cases, this alone did not significantly affect the overall classification, as the binarized images in row c) show.

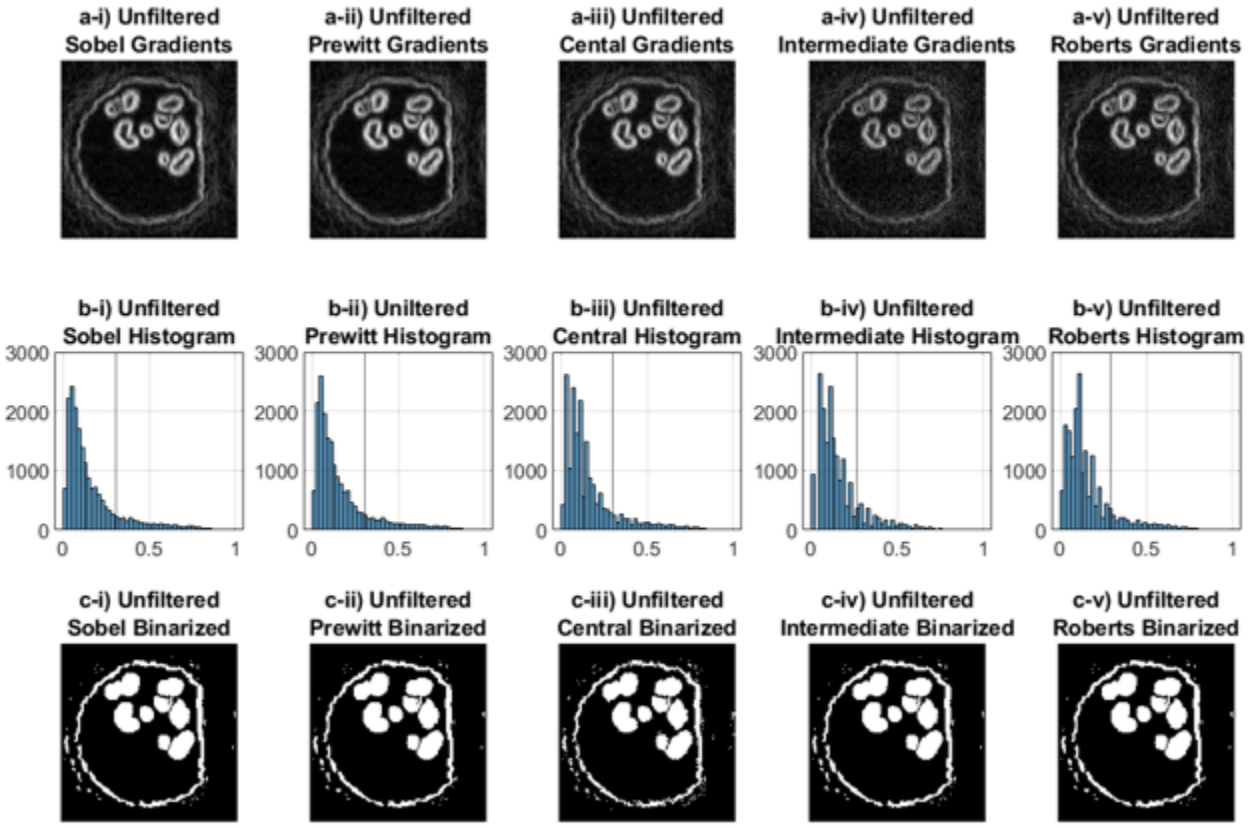

Figure 8: Results of applying gradients to unfiltered image. Rescaled gradients images are shown in the first row (a), gradient histograms with threshold in the second (b), and binarized and filled images in the third (c).

3.3 Filtering – Qualitative

Results from applying different filters can be qualitatively observed in Figure 8. Compared to the effects of different gradients seen in Figure 7, the different filters resulted in more significant differences than different gradients. First, the median filter resulted in smaller gradient magnitudes. This can be observed in the dimmer image in Figure 8a-ii) and the skewed histogram in Figure 8b-ii). This skewing of gradient magnitudes resulted in the threshold value having a much more significant impact than the other filters because changes in the threshold value affected a greater percentage of pixels, causing more instances of significant under classification (missing pores). Additionally, the threshold values were significantly lower than those of the other filtering methods, as the median-filtered images had thresholds close to 0.1 while the other methods had thresholds between 0.25 and 0.3. Second, the gaussian filter resulted in a smoother gradient image. This also resulted in a more distributed histogram of gradient magnitudes and therefore lowered the sensitivity to the threshold value, making classification more accurate in detecting the presence of forming pores. Compared to the other filters, the gaussian filter images and histograms looked most like the unfiltered images but with slightly greater gradient magnitudes (shown by brighter pixels in the gradient image). Finally, the anisotropic filter resulted in the smoothest gradient images. This reduced the quantity of noisy pixels while still maintaining the major grayscale value changes between solid part and forming pore. Additionally, this resulted in smoother edges of the final pores as seen in Figure 8c-iv). However, this did decrease the smooth distribution of

magnitudes in the histogram in Figure 8b-iv), resulting in local threshold sensitivities. Contrary to the sensitivity seen with the median filter, though, this provided magnitudes that allowed for easier classification, as each jump in counts was typically due to different classes (sintered powder, melted powder, contour, or forming pore). These effects resulted in some changes in the final binarized images in row c). The anisotropic filter resulted in the smoothest pore edges and the least noise, and the gaussian filter also resulted in more smooth edges and reduced noise. The median filter did reduce noise in some cases, but it also resulted in severe under-classification in other cases due to the significant skewing of gradient values.

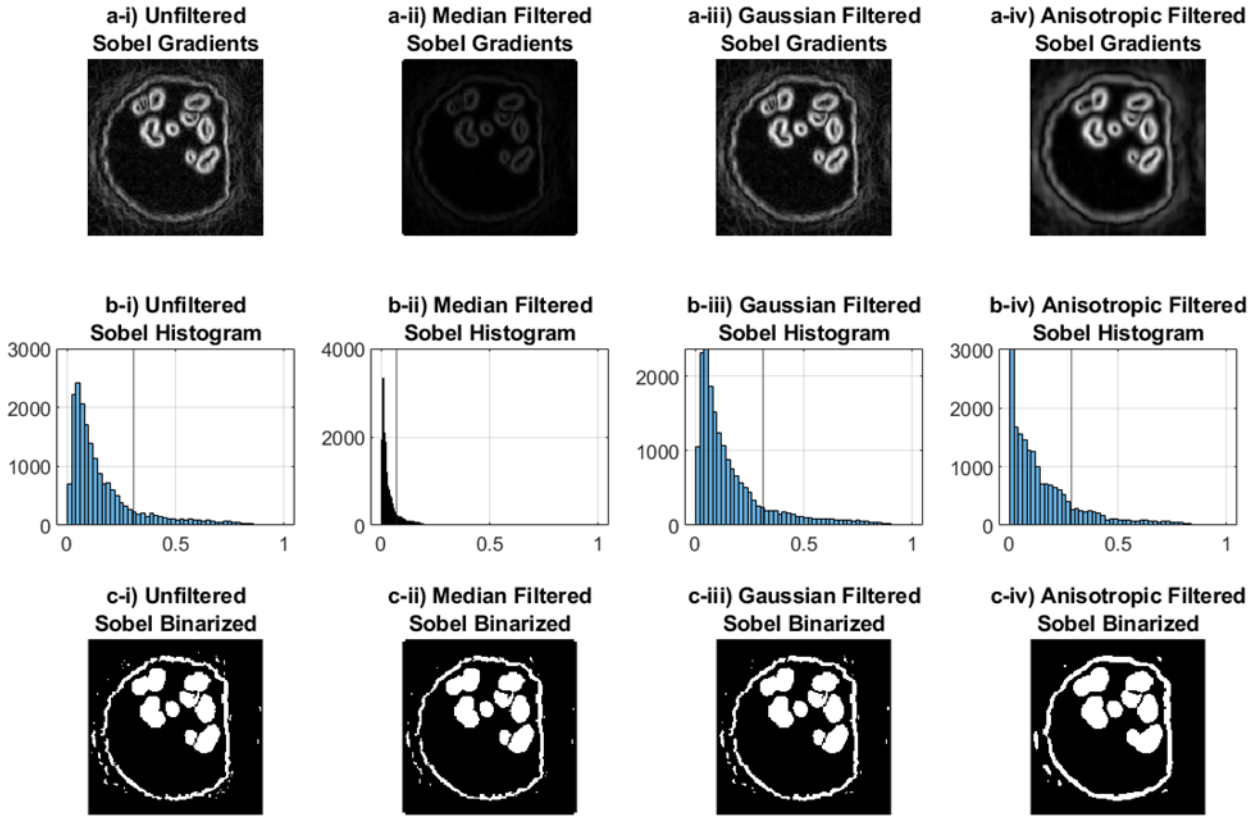

Figure 9: Results from applying filters to Sobel gradient. Gradient images are shown in the first row (a), gradient histograms with thresholds in the second row (b), and binarized images in the third row (c).

3.4 Gradient – Quantitative

To quantitatively evaluate the various combinations of gradients and filters, a G-Mean for each image was calculated. Due to the severe imbalance of the positive and negative classes, this metric was optimal because it treats each class as separate accuracy percentages (Equations 1-2) before combining into a single metric (Equation 3).

$$= \frac{\qquad\qquad}{+} \tag{1}$$

$$= \frac{\qquad\qquad}{+} \tag{2}$$

$$= \frac{\qquad}{\times} \tag{3}$$

Figure 9 shows all results of the quantitative comparison analysis, grouped together by gradient type. The first major observation is the effect of porosity levels (caused by varying FO levels). The medium porosity (FO = 65 mA) samples had the highest performance, the high porosity (FO = 75 mA) had the second highest performance, and the low porosity (FO = 55 mA) had the lowest performance. Additionally, each porosity level different levels of variability, as the high porosity samples had similar performance results for all gradients. The medium porosity samples followed that trend for the Sobel and Prewitt gradients, but there were some samples that had sharp decreases in performance using the median filter with the other 3 gradient types (discussed more in Section 3.5). The low porosity samples had more variability between individual samples, but the results were still relatively consistent for the Sobel and Prewitt gradient types. However, like with the medium porosity samples, the performance varied more with the other 3 gradient types, especially when used with the median filter.

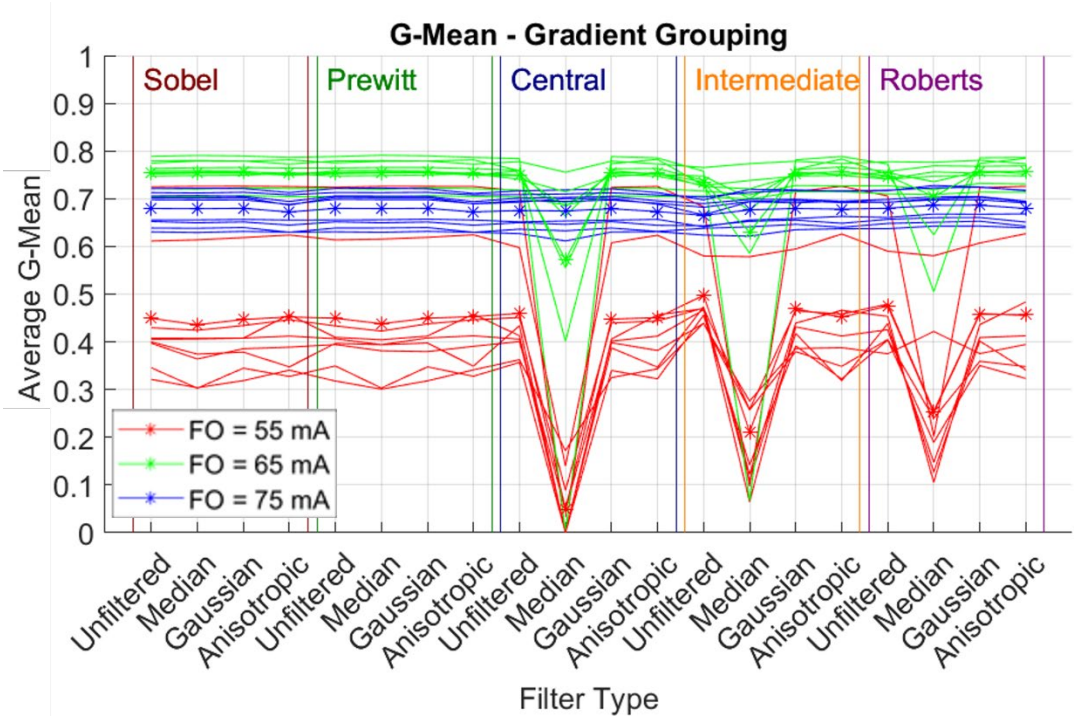

Figure 10: Results of quantitative analysis, grouped together by gradient type. Solid lines show results for individual samples, while stars show average for each FO value

These results are condensed in Figure 10. These results were obtained by taking the average (Figure 10a) and standard deviation (Figure 10b) for all images processed with that gradient type (all samples, all filters). Here, it is easier to see that Sobel and Prewitt gradients had both higher average G-Mean and lower standard deviation values. This increase in performance is inversely proportional to porosity levels, as samples with higher porosity had more similar G-Mean values, meaning the gradient type had less impact.

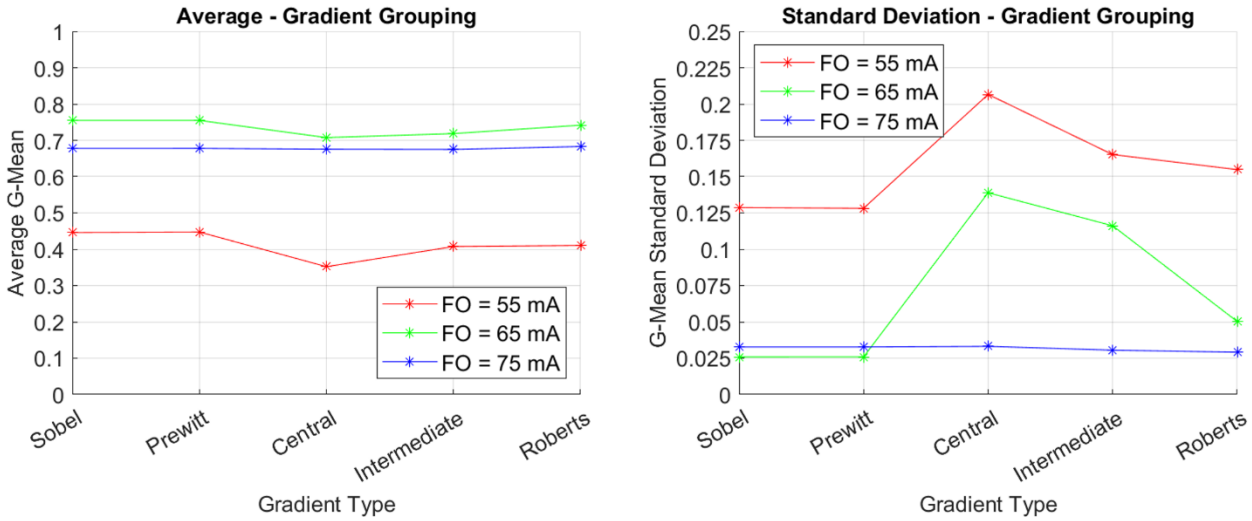

Figure 11: Plots of a) average G-Mean and b) G-Mean standard deviation for each gradient type

3.5 Filtering – Quantitative

All results are once again plotted in Figure 11, this time grouped together by filter type. Once again, it should be noted the effect porosity level has on the performance. However, with this new grouping, it is clearer the median filter resulted in a significant decrease in performance for all low porosity and most medium porosity samples. The unfiltered images had significantly less variability than the median filter, but there were still some differences between samples and gradient types. However, the gaussian and anisotropic filters resulted in relatively homogeneous results. The anisotropic filtering resulted in nearly the same average G-Mean values for all gradient types. However, even though the results were the same for each sample, there was a greater difference between the different samples' values, increasing the variance. This behavior is seen the most in the low porosity samples and some in the medium porosity. However, like with the gradients, the high porosity samples did not see significant impact from different filters.

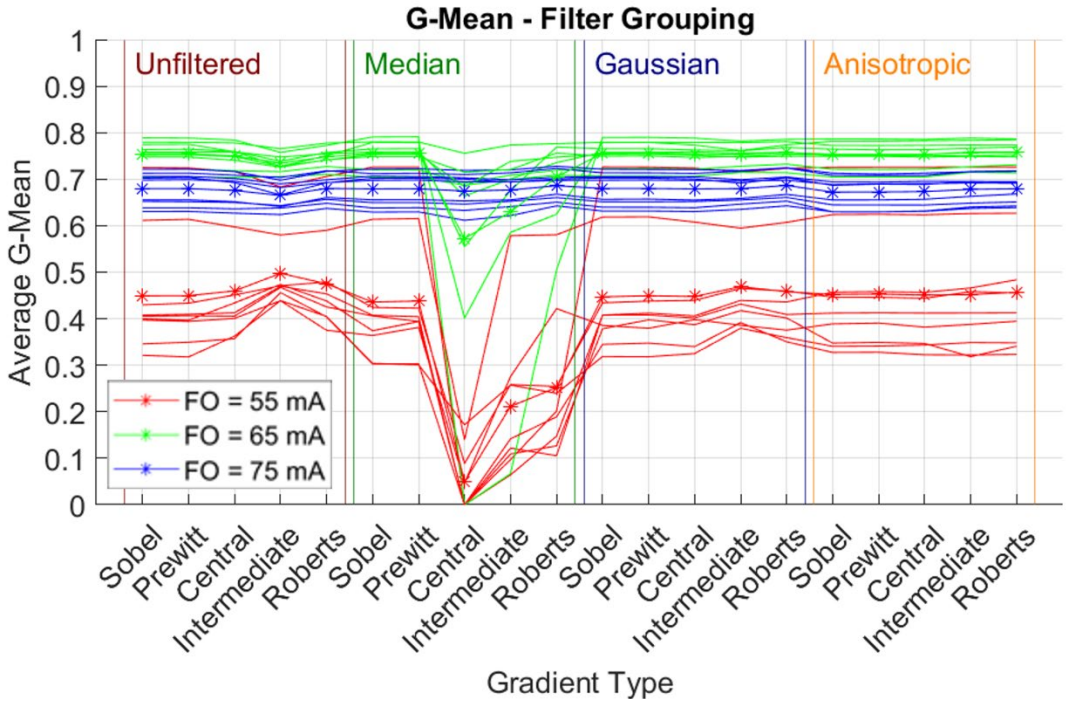

Figure 12: Results of quantitative analysis, grouped together by filter type. Solid lines show results for individual samples, while stars show average for each FO value

These observations are confirmed by the condensed plots in Figure 12. The median filter resulted in lower averages and higher standard deviations for both the low and medium porosity values, while the averages and standard deviations for the unfiltered, gaussian, and anisotropic filters were relatively close. Meanwhile, the high porosity samples again saw minimal impact from the different filters, having nearly the same average and low standard deviation values.

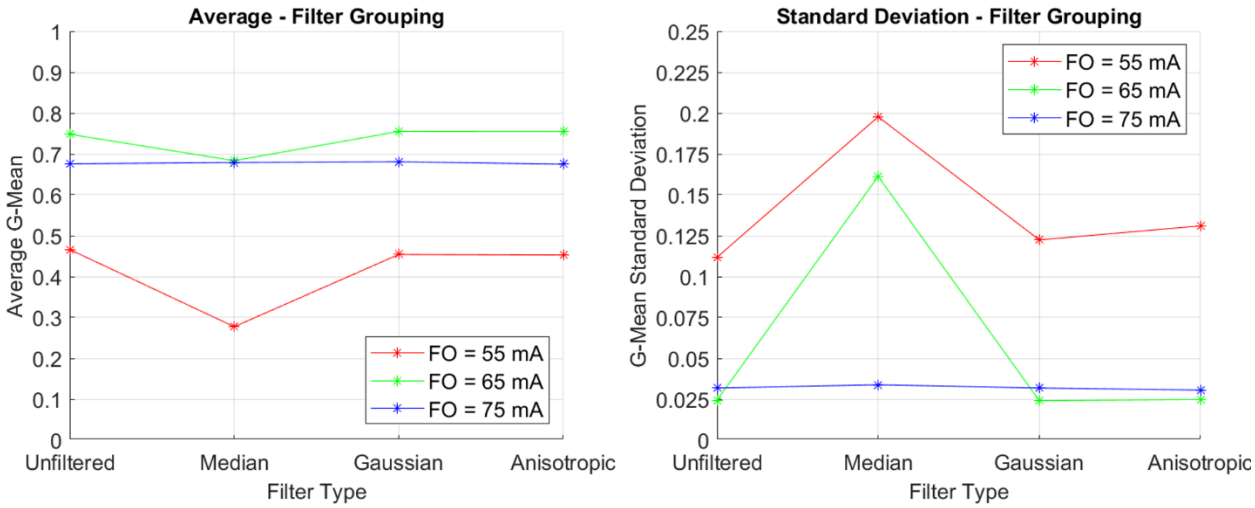

Figure 13: Plots of a) average G-Mean and b) G-Mean standard deviation for each filter type

4. Discussion

****

As previously stated, the porosity levels had the most impact on porosity. This is likely due to two main factors. The first is micropores. Due to the high resolution of the XCT scanning, there were smaller micropores detected that were only a few pixels in size. Because they were so small, it was unlikely that they would appear in the IR images with their much larger pixel size. These micropores were present in all samples. However, since the low porosity samples had fewer total pores, these micropore pixels consisted of a higher percentage of the total number of pore pixels and resulted in a lower sensitivity for these samples. Luckily, many of these pores could be closed with a post-processing step, like hot isostatic pressing, so future applications could simply filter out these micropores based on post-processing capabilities. The second is pore oversizing. As detailed in Section 3.2 and 3.3, the pores in the IR images were larger than those in the XCT scans due to different pixel/voxel sizes and heat dissipation. Therefore, when more pores were present, a larger percentage of the overall area was covered, capturing most of the pore pixels but also incorporating large amounts of surround pixels. This reduced variance by consistently covering most of the available area, capturing any micropores and helping detect nearby pores that may have been missed. This is the reason many algorithms focus on pore-to-pore detection instead of pixel-to-pixel [26], but this can be addressed through additional research into how the pores change in shape and size from in-situ IR images to ex-situ XCT scans.

Gradients, on the other hand, did not play as large of a role. As described in Section 3.4, the Sobel and Prewitt gradients had slightly higher averages and lower standard deviations, meaning they were slightly more accurate with less variance. This was likely due to these gradients using a larger kernel size for calculations, as they both use a 3-by-3 kernel size as opposed to the 2-by-2 or even 1-by-2 sizes for the other gradient types. With a larger kernel size, more neighboring pixels were utilized, making the calculations less dependent on any outlying individual pixels that may skew results. This behavior was more pronounced with lower porosity levels, especially with the lower overall gradient magnitudes from the median filter, as these smaller kernels could not account for the reduced change in grayscale value between pixels. Therefore, the gradients with the larger kernel sizes should be used for more accurate and consistent.

Finally, filtering also did not play as large of a role as focus offset. The gaussian and anisotropic filters had roughly the same performance as the unfiltered, with very similar average and standard deviation G-Mean values. The gaussian filter reduced the number of noisy pixels while remaining closest to the unfiltered image appearance, though this would include both good and bad features such as rough edges. The anisotropic filter resulted in significantly smoother edges and clearer gradients, which at first should seem to lead to better performance. Unfortunately, this led to a bit of pore oversizing, bringing the performance back down. The median filter, however, did significantly decrease the performance of both the low and medium porosity levels, especially with the Central, Intermediate, and Roberts gradients. This result is understandable, as median filters are intended to reduce individual pixels that vary drastically from the nearby pixels (called salt and pepper noise), but this results in bringing all the pixel values too close together, reducing the gradient magnitudes. The gaussian and anisotropic filters, on the other hand, are intended to remove noise while maintaining feature edges, which allow the gradient magnitudes to remain high enough for easier detection. This is why their performance was close

to that of unfiltered images. Therefore, if filtering will be used in future applications, filters like a gaussian or anisotropic filter should be used.

5. Conclusion

****

In this work, a gradient-based segmentation process was analyzed for its effectiveness in detecting and modeling porosity from in-situ IR images in PBF-EB processes. This process was analyzed with 5 different gradient calculations and 4 different prefiltering types, and each combination of gradient and prefilter was evaluated using XCT scans as ground-truth verification. Some conclusions from the work include:

- Most gradient types had similar effects on porosity detection and modeling. The gradient types with 3-by-3 sized kernels, such as the Sobel and Prewitt, tended to perform slightly more accurately (larger average) and reliably (smaller variance), but the average performance was similar between all 5 gradient types.
- Gaussian and anisotropic filters had similar performance to the unfiltered, with differences being mostly qualitative and did not result in significant increase in performance. The median filter, however, resulted in significantly lower performance due to the significant grayscale value skewing.
- Porosity levels and density had the largest effect on overall results. Since the IR images were taken with a larger pixel size than the XCT voxel size, the pores appeared larger in the IR images. Therefore, higher levels of porosity resulted in a higher false positive count and lower overall accuracy. However, higher porosity levels also covered a larger proportion of the overall area, resulting lower variance and meaning the detection algorithm was more consistent.

These results provide a worthwhile starting point for machine operators looking to detect porosity in in-situ IR images in both research and industry. The image processing recommendations can be used either on their own or as part of a larger algorithm detecting a variety of defects for either post-build part quality assessment or in-situ closed-loop process control. If used on their own, further research should be done comparing the different sizes of the pores in the two datasets and determine how different factors (different pixel/voxel sizes, heat dissipation, etc.) quantitatively affect detection accuracy. Finally, the scope of this work only included one material and layer thickness, which can both affect emissivity, so the effect of different materials and layer thicknesses on detection and porosity formation can be studied in further research.

Acknowledgements

The authors would like to acknowledge the Department of Energy Grant DE-EE0008303 and Eaton Aerospace for funding the materials and labor costs associated with this work. The authors would also like to thank Dr. Jaime Berez (UNC-Charlotte), Dr. Elliott Jost (Lockheed Martin), and Caroline Massey (Georgia Institute of Technology) for their help with designing the fixturing and registration processes for previous work that have since been adapted in this paper.

References

[1] B. Blakey-Milner *et al.*, "Metal additive manufacturing in aerospace: A review," *Mater.*

Des., vol. 209, p. 110008, 2021, doi: 10.1016/j.matdes.2021.110008.
[2] M. Salmi, "Additive manufacturing processes in medical applications," *Materials (Basel).*, vol. 14, no. 1, pp. 1–16, 2021, doi: 10.3390/ma14010191.
[3] F. H. Kim and S. P. Moylan, "Literature Review of Metal Additive Manufacturing Defects," *NIST Adv. Manuf. Ser.*, pp. 1–17, 2018, [Online]. Available: http://nvlpubs.nist.gov/nistpubs/ams/NIST.AMS.100-16.pdf.
[4] F. Caltanissetta, M. Grasso, S. Petrò, and B. M. Colosimo, "Characterization of in-situ measurements based on layerwise imaging in laser powder bed fusion," *Addit. Manuf.*, vol. 24, pp. 183–199, Nov. 2018, doi: 10.1016/j.addma.2018.09.017.
[5] M. G. Guerra, V. Errico, A. Fusco, F. Lavecchia, S. L. Campanelli, and L. M. Galantucci, "High resolution-optical tomography for in-process layerwise monitoring of a laser-powder bed fusion technology," *Addit. Manuf.*, vol. 55, no. February, p. 102850, 2022, doi: 10.1016/j.addma.2022.102850.
[6] P. J. DePond *et al.*, "In situ measurements of layer roughness during laser powder bed fusion additive manufacturing using low coherence scanning interferometry," *Mater. Des.*, vol. 154, pp. 347–359, 2018, doi: 10.1016/j.matdes.2018.05.050.
[7] L. Scime, D. Siddel, S. Baird, and V. Paquit, "Layer-wise anomaly detection and classi fi cation for powder bed additive manufacturing processes : A machine-agnostic algorithm for real-time pixel- wise semantic segmentation," *Addit. Manuf.*, vol. 36, no. July, p. 101453, 2020, doi: 10.1016/j.addma.2020.101453.
[8] M. Bugatti and B. M. Colosimo, "The intelligent recoater: A new solution for in-situ monitoring of geometric and surface defects in powder bed fusion," *Addit. Manuf. Lett.*, vol. 3, no. March, p. 100048, 2022, doi: 10.1016/j.addlet.2022.100048.
[9] T. Craeghs, S. Clijsters, and J. Kruth, "Online Quality Control of Selective Laser Melting," *Phys. Rev. E*, pp. 212–226, 2011, [Online]. Available: http://www.ainfo.inia.uy/digital/bitstream/item/7130/1/LUZARDO-BUIATRIA-2017.pdf.
[10] R. J. Williams *et al.*, "In situ thermography for laser powder bed fusion: Effects of layer temperature on porosity, microstructure and mechanical properties," *Addit. Manuf.*, vol. 30, no. October, p. 100880, 2019, doi: 10.1016/j.addma.2019.100880.
[11] M. Bisht, N. Ray, F. Verbist, and S. Coeck, "Correlation of selective laser melting-melt pool events with the tensile properties of Ti-6Al-4V ELI processed by laser powder bed fusion," *Addit. Manuf.*, vol. 22, no. May, pp. 302–306, 2018, doi: 10.1016/j.addma.2018.05.004.
[12] A. du Plessis, I. Yadroitsava, and I. Yadroitsev, "Effects of defects on mechanical properties in metal additive manufacturing: A review focusing on X-ray tomography insights," *Mater. Des.*, vol. 187, p. 108385, 2020, doi: 10.1016/j.matdes.2019.108385.
[13] H. Gaja and F. Liou, "Defects monitoring of laser metal deposition using acoustic emission sensor," *Int. J. Adv. Manfuacturing Technol.*, p. 14, 2017, doi: 10.1007/s00170-016-9366-x.
[14] H. Rieder, M. Spies, J. Bamberg, and B. Henkel, "On- and Offline Ultrasonic Inspection of Additively Manufactured Components," *19th World Conf. Non-Destructive Test.*, pp. 1–8, 2016, [Online]. Available: http://www.ndt.net/article/wcndt2016/papers/th2e1.pdf.
[15] J. Whiting *et al.*, *Powder Spreading Testbed for Studying the Powder Spreading Process in Powder Bed Fusion Machines*, no. December. 2023.
[16] H. C. de Winton, F. Cegla, P. A. Hooper, H. C. de Winton, F. Cegla, and P. A. Hooper, "A method for objectively evaluating the defect detection performance of in-situ

monitoring systems," *Addit. Manuf.*, vol. 48, p. 102431, Dec. 2021, doi: 10.1016/j.addma.2021.102431.
[17] "Layerwise Automated Visual Inspection in Laser Powder-Bed Additive Manufacturing," pp. 1–9, 2015, doi: https://doi.org/10.1115/MSEC2015-9393.
[18] S. Moylan, E. Whitenton, B. Lane, and J. Slotwinski, "Infrared thermography for laser-based powder bed fusion additive manufacturing processes," in *40TH ANNUAL REVIEW OF PROGRESS IN QUANTITATIVE NONDESTRUCTIVE EVALUATION: Incorporating the 10th International Conference on Barkhausen Noise and Micromagnetic Testing*, Oct. 2014, pp. 1191–1196, doi: 10.1063/1.4864956.
[19] H. Krauss, T. Zeugner, and M. F. Zaeh, "Layerwise Monitoring of the Selective Laser Melting Process by Thermography," *Phys. Procedia*, vol. 56, pp. 64–71, Sep. 2014, doi: 10.1016/j.phpro.2014.08.097.
[20] H. Gong, K. Rafi, N. V. Karthik, T. Starr, and B. Stucker, "Defect morphology in Ti-6Al-4V parts fabricated by Selective Laser Melting and Electron Beam Melting," *24th Int. SFF Symp. - An Addit. Manuf. Conf. SFF 2013*, no. July 2015, pp. 440–453, 2013, doi: 10.26153/tsw/15566.
[21] Z. C. Cordero, R. B. Dinwiddie, D. Immel, and R. R. Dehoff, "Nucleation and growth of chimney pores during electron-beam additive manufacturing," *J. Mater. Sci.*, vol. 52, no. 6, pp. 3429–3435, 2017, doi: 10.1007/s10853-016-0631-z.
[22] E. Rodriguez, J. Mireles, C. A. Terrazas, D. Espalin, M. A. Perez, and R. B. Wicker, "Approximation of absolute surface temperature measurements of powder bed fusion additive manufacturing technology using in situ infrared thermography," *Addit. Manuf.*, vol. 5, pp. 31–39, 2015, doi: 10.1016/j.addma.2014.12.001.
[23] M. Mahmoudi, A. A. Ezzat, and A. Elwany, "Layerwise Anomaly Detection in Laser Powder-Bed Fusion Metal Additive Manufacturing," vol. 141, no. March, pp. 1–13, 2019, doi: 10.1115/1.4042108.
[24] C. S. Lough *et al.*, "Correlation of SWIR imaging with LPBF 304L stainless steel part properties," *Addit. Manuf.*, vol. 35, no. May, p. 101359, 2020, doi: 10.1016/j.addma.2020.101359.
[25] S. Yoder *et al.*, "Characterization of topology optimized Ti-6Al-4V components using electron beam powder bed fusion," *Addit. Manuf.*, vol. 19, pp. 184–196, 2018, doi: 10.1016/j.addma.2017.12.001.
[26] L. Scime and J. Beuth, "Using machine learning to identify in-situ melt pool signatures indicative of flaw formation in a laser powder bed fusion additive manufacturing process," *Addit. Manuf.*, vol. 25, no. October 2018, pp. 151–165, 2019, doi: 10.1016/j.addma.2018.11.010.
[27] D. Kozjek, F. M. Carter, C. Porter, J. E. Mogonye, K. Ehmann, and J. Cao, "Data-driven prediction of next-layer melt pool temperatures in laser powder bed fusion based on co-axial high-resolution Planck thermometry measurements," *J. Manuf. Process.*, vol. 79, no. April, pp. 81–90, 2022, doi: 10.1016/j.jmapro.2022.04.033.
[28] J. L. Bartlett, F. M. Heim, Y. V. Murty, and X. Li, "In situ defect detection in selective laser melting via full-field infrared thermography," *Addit. Manuf.*, vol. 24, no. July, pp. 595–605, 2018, doi: 10.1016/j.addma.2018.10.045.
[29] R. Cunningham, S. P. Narra, C. Montgomery, J. Beuth, and A. D. Rollett, "Synchrotron-Based X-ray Microtomography Characterization of the Effect of Processing Variables on Porosity Formation in Laser Power-Bed Additive Manufacturing of Ti-6Al-4V," *Jom*, vol.

69, no. 3, pp. 479–484, 2017, doi: 10.1007/s11837-016-2234-1.
[30] J.-B. Forien, N. P. Calta, P. J. DePond, G. M. Guss, T. T. Roehling, and M. J. Matthews, “Detecting keyhole pore defects and monitoring process signatures during laser powder bed fusion: a correlation between in situ pyrometry and ex situ X-ray radiography,” *Addit. Manuf.*, p. 101336, 2020, doi: 10.1016/j.addma.2020.101336.
[31] S. Feng, Z. Chen, B. Bircher, Z. Ji, L. Nyborg, and S. Bigot, “Predicting laser powder bed fusion defects through in-process monitoring data and machine learning,” *Mater. Des.*, vol. 222, 2022, doi: 10.1016/j.matdes.2022.111115.
[32] G. Croset, G. Martin, C. Josserond, P. Lhuissier, J. J. Blandin, and R. Dendievel, “In-situ layerwise monitoring of electron beam powder bed fusion using near-infrared imaging,” *Addit. Manuf.*, vol. 38, Feb. 2021, doi: 10.1016/j.addma.2020.101767.
[33] J. Petrich, Z. Snow, D. Corbin, and E. W. Reutzel, “Multi-modal sensor fusion with machine learning for data-driven process monitoring for additive manufacturing,” *Addit. Manuf.*, vol. 48, no. PB, p. 102364, 2021, doi: 10.1016/j.addma.2021.102364.
[34] L. A. Shepp and B. F. Logan, “Fourier Reconstruction of a Head Section.,” *IEEE Trans. Nucl. Sci.*, vol. NS-21, no. 3, pp. 21–43, 1974, doi: 10.1109/tns.1974.6499235.
[35] I. Arganda-Carreras *et al.*, “Trainable Weka Segmentation: A machine learning tool for microscopy pixel classification,” *Bioinformatics*, vol. 33, no. 15, pp. 2424–2426, 2017, doi: 10.1093/bioinformatics/btx180.
[36] J. C. Miers, D. G. Moore, and C. Saldana, “Defect Evolution in Tensile Loading of 316L Processed by Laser Powder Bed Fusion,” *Exp. Mech.*, vol. 62, no. 6, pp. 969–983, 2022, doi: 10.1007/s11340-021-00815-5.
[37] N. Otsu, “A Threshold Selection Method from Gray-Level Histograms,” *IEEE Trans. Syst. Man. Cybern.*, vol. C, no. 1, pp. 62–66, 1979.